ACS APPLIED MATERIALS & INTERFACES

Research Article

Cite This: ACS Appl. Mater. Interfaces 2017, 9, 36962-36970

www.acsami.org

Efficient Suppression of Defects and Charge Trapping in High Density In−Sn−Zn−O Thin Film Transistor Prepared using Microwave-Assisted Sputter

Youngin Goh,[†] Jaehan Ahn,[‡] Jeong Rak Lee,[§] Wan Woo Park,[§] Sang-Hee Ko Park,*[,‡] and Sanghun Jeon*[,†]

[†]Department of Applied Physics, Korea University, 2511, Sejongro, Sejong, 339-700, Republic of Korea

[‡]Department of Material Science and Engineering, Korea Advanced Institute of Science and Technology, 291 Daehakro, Yuseong-gu, Daejeon, 305-701, Republic of Korea

[§]Advanced Vacuum and Clean Equipment Optimizer (AVACO), Woelam-dong, Dalseo-gu, Daegu, 1107, Republic of Korea

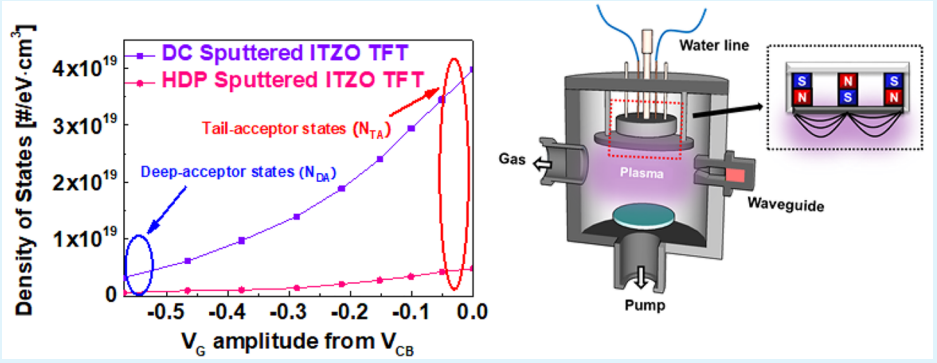

ABSTRACT: Amorphous oxide semiconductor-based thin film transistors (TFTs) have been considered as excellent switching elements for driving active-matrix organic light-emitting diodes (AMOLED) owing to their high mobility and process compatibility. However, oxide semiconductors have inherent defects, causing fast transient charge trapping and device instability. For the next-generation displays such as flexible, wearable, or transparent displays, an active semiconductor layer with ultrahigh mobility and high reliability at low deposition temperature is required. Therefore, we introduced high density plasma microwave-assisted (MWA) sputtering method as a promising deposition tool for the formation of high density and high-performance oxide semiconductor films. In this paper, we present the effect of the MWA sputtering method on the defects and fast charge trapping in In−Sn−Zn−O (ITZO) TFTs using various AC device characterization methodologies including fast *I*−*V*, pulsed *I*−*V*, transient current, low frequency noise, and discharge current analysis. Using these methods, we were able to analyze the charge trapping mechanism and intrinsic electrical characteristics, and extract the subgap density of the states of oxide TFTs quantitatively. In comparison to conventional sputtered ITZO, high density plasma MWA-sputtered ITZO exhibits outstanding electrical performance, negligible charge trapping characteristics and low subgap density of states. High-density plasma MWA sputtering method has high deposition rate even at low working pressure and control the ion bombardment energy, resulting in forming low defect generation in ITZO and presenting high performance ITZO TFT. We expect the proposed high density plasma sputtering method to be applicable to a wide range of oxide semiconductor device applications.

KEYWORDS: *oxide semiconductor, thin film transistor, In−Sn−Zn-O, microwave-assisted sputter, high density plasma, charge trapping, defect density, reflected Ar*

1. INTRODUCTION

Oxide semiconductor-based thin film transistors (TFTs) have attracted immense attention as switching devices for next-generation flexible displays owing to their superior electrical and optical properties, low-temperature process accessibility, and process compatibility with the previous display technologies.[1−4] Since the introduction of In−Ga−Zn-O by Hosono group, *c*-axis crystalline oxide and other amorphous semiconductors, such as In−Zn−O, Hf−In−Zn−O, In−Sn−Zn-O, Al−Sn−Zn−, and Al−In−Sn−Zn−O, have been studied intensively.[5−9] Among them, In−Sn−Zn−O (ITZO) materials have strong advantages of transparency and high mobility. However, ultrahigh field-effect mobility and high-reliability are required for the industrial applications of high resolution, high frame rate and large area display.[10−14] By using the conventional sputter, it is difficult to deposit high-quality oxide

Received: June 6, 2017
Accepted: October 6, 2017
Published: October 6, 2017

DOI: 10.1021/acsami.7b08065
ACS Appl. Mater. Interfaces 2017, 9, 36962−36970

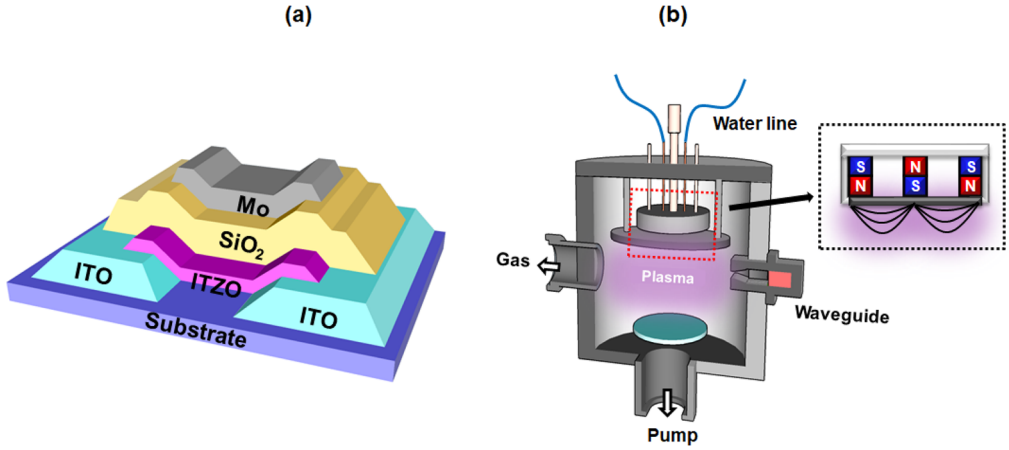

Figure 1. (a) Schematics of ITZO TFT. (b) Schematics of high density sputtering system.

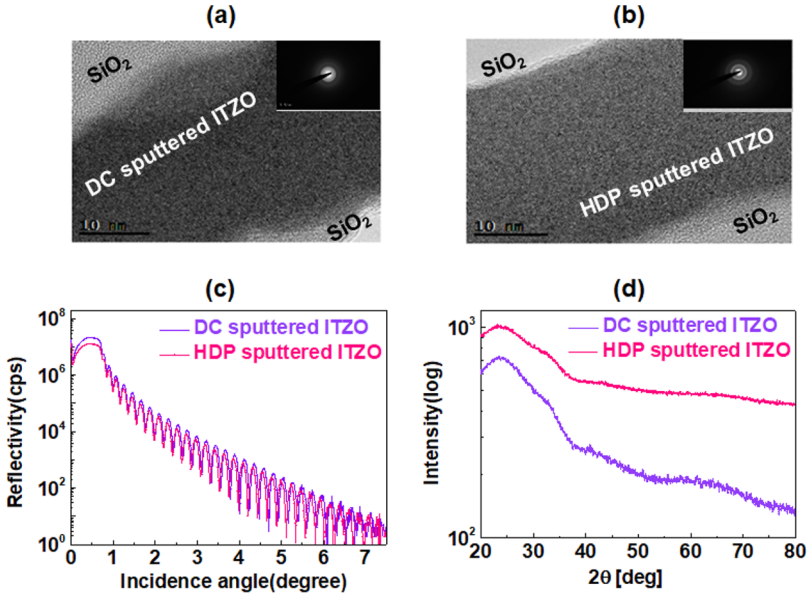

Figure 2. Transmission electron microscopy (TEM) image of (a) DC sputtered ITZO TFT and (b) HDP sputtered ITZO TFT. (c) X-ray reflectivity spectroscopy(XRR) data of both DC sputtered ITZO and HDP sputtered ITZO. (d) X-ray diffraction spectroscopy(XRD) data of both DC sputtered ITZO and HDP sputtered ITZO.

semiconductor film. Therefore, to produce high-quality and high-performance ITZO films, we introduced the concept of sputter, that is, microwave-assisted sputter (MWA sputter).[15,16] We confine high-density plasma with the induction of microwave into the DC magnetron sputter by using the electron cyclotron resonance (ECR) effect. The MWA sputtering method has the advantages of producing highly ionized plasma, managing working pressure and controlling reflected Ar bombardment energy. Moreover, it enables low deposition temperatures, low discharge voltage and high deposition rate.[16−18] Consequently, by utilizing MWA sputtering, it is possible to produce high-quality metal oxide films even at room temperature, rendering the most powerful candidates for next-generation displays possible. We applied MWA sputtering to the deposition of ITZO films. Consequently, the material properties and device performance of oxide semiconductors are significantly enhanced, resulting in high field-effect mobility, negligible fast transient charging effect and less subgap density of states.

In this Research Article, we report the materials and structural properties of high-density plasma ITZO films deposited via MWA sputter using transmission electron microscopy (TEM) image, X-ray reflectivity spectroscopy (XRR) and X-ray diffraction spectroscopy (XRD). Furthermore, we demonstrate the effect of MWA sputtering method on the characteristic of ITZO films by analyzing the defects and fast charge trapping mechanism when compared to typical DC sputtered In−Sn−Zn−O films. Here, we employ various electrical characterization methods including microsecond fast *I*−*V*, pulsed *I*−*V*, transient current, low frequency noise analysis, and discharge current analysis (DCA) to identify the defect sites and charge trapping effects quantitatively. From these analyses, we conclude that the MWA sputter method enables the deposition of high-quality and the formation of high-performance ITZO TFTs under low deposition temperature and low working pressure, which is an attractive study for the realization of next-generation flexible and transparent displays.

DOI: 10.1021/acsami.7b08065
ACS Appl. Mater. Interfaces 2017, 9, 36962−36970

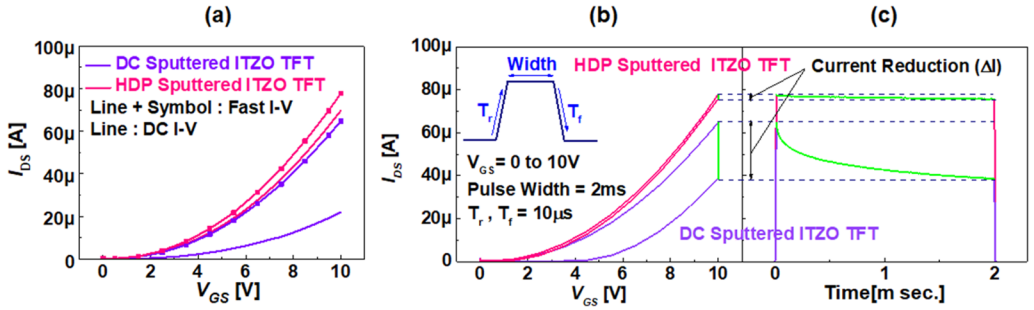

Figure 3. (a) Fast $I-V$ and typical DC $I-V$ curves of DC ITZO and HDP ITZO TFTs. (b) Representative single-pulse $I-V$ (rising time = falling time = 10 μs and pulse width = 2 ms) curves of DC ITZO and HDP ITZO TFTs. (c) Corresponding transient current versus time data of DC ITZO and HDP ITZO TFTs.

2. EXPERIMENTAL METHODS

2.1. Device Fabrication. A schematic of the fabricated oxide TFT with a top-gated, top-contact structure is presented in Figure 1a. Mo metal was used as the gate via sputtering and 150 nm-thick transparent ITO layers were deposited as the source and drain via sputtering. A 120 nm-thick SiO_2 layer, which was deposited by using plasma-enhanced chemical vapor deposition, was used as the gate insulator. For an active semiconductor, 40 nm-thick In−Sn−Zn−O metal oxide film was prepared using two different methods, such as conventional DC magnetron and high-density plasma (HDP) sputtering methods with MWA sputter. The same equipment has been used for MWA and conventional DC sputter. The only difference between two methods is the presence of microwave transfer for MWA method. Therefore, all the hardware, such as distance between target and substrate, position of target and structure of equipment, are the same. The MWA sputter is based on a typical DC magnetron sputter, but microwave is introduced into the chamber through a waveguide and the electron cyclotron resonance (ECR) effect is utilized as shown in Figure 1b. A magnet is placed on the target for confining the plasma effectively. When charged particles are in magnetic field, they receive the Lorentz force, $\vec{F} = q(\vec{v} \times \vec{B})$. According to this formula, when they move in a direction perpendicular to the magnetic field, the Lorentz force acts as a centripetal force to perform the circular motion. The electrons performing the circular motion have the following angular frequency

$$\omega_{ce} = \frac{qB}{m_e}$$

where ω_{ce} is angular frequency of the electrons rotating by the magnetic field, q is elementary charge, and B is intensity of magnetic field. Then, if a microwave having the same frequency as the electron is applied, the resonance occurs and electrons have maximum energy. The chain collision phenomenon caused by the electron movement ionizes or excites the neutral gas to form a high-density plasma. This is the basic principle of electron cyclotron resonance (ECR). The electron cyclotron frequency (or gyro motion frequency) is controlled by the magnet to match the microwave frequency.[13−15] In these research, we set the magnitude of the magnet to 875 G, and frequency of microwave to 2.45 GHz. The ECR condition facilitates the electron and ion to absorb the microwave energy efficiently, thus inducing high-density plasma and high deposition rate even at low operation pressure. Accordingly, the deposition rates were 6.55 and 11.3 Å/s in the case of the DC sputter and MWA sputter, respectively. Moreover, the operator pressure of conventional DC sputtering and ECR sputtering is 3 mTorr and 0.6 mTorr, respectively. We used Ar and O_2 gas in the sputtering, and oxygen partial pressure is 40%. The post annealing was performed at 350 °C for 2 h in vacuum. Also, the channel length and width of device is 40 and 20 μm, respectively.

2.2. Material Analysis. Figures 2a and 2b show the TEM images of the DC sputtered ITZO film and HDP sputtered ITZO film, respectively. From these images, we confirmed that the HDP sputtered ITZO film was deposited more uniformly and clearly as compared to the DC sputtered ITZO film. In the inset of Figure 2, the transmission electron diffraction pattern images of the ITZO metal oxide films show a hazy image, indicating that the prepared film was formed in an amorphous phase. To verify the effect of MWA sputter on the properties of the film, we also examined the results of XRR and XRD. From the XRR data shown in Figure 2c, we found that the density was 6.91 and 7.02 g/cm^3 for the ITZO film deposited by typical DC magnetron sputter and ITZO film deposited by MWA sputter, respectively, indicating that the MWA sputter induces high-density plasma and produces high-density oxide semiconductor films. From the XRD data shown in Figure 2d, we identified that both the ITZO films have an amorphous phase, which is consistent with the diffraction pattern.

2.3. Electrical Analysis. To evaluate the electrical characteristics of ITZO TFTs, we employed various AC device analysis methods. For fast-pulse methods including fast $I-V$, pulsed $I-V$, transient current, and low-frequency noise analysis, we used the semiconductor parameter analyzer (Agilent B1500) with a waveform generator/fast measurement unit (WGFMU). TFTs have a designed capacitor and a parasitic capacitor. Considering of the thickness and the dielectric constant of gate insulator as well as other parameters, the RC delay time constant is less than a few nano second. We set the minimum pulse rising time to 1 μs which can ignore the RC delay effect. Furthermore, DCA was carried out using a pulse generator (Agilent 81104A) and a source meter (Keithley 2401), which is controlled by Lab-view program.

3. RESULTS AND DISCUSSION

To investigate the effect of the MWA sputter method on the characteristics of In−Sn−Zn−O TFTs, we performed DC $I-V$ and fast $I-V$ measurements using a semiconductor parameter analyzer and a WGFMU. A typical DC $I-V$ measurement method takes a long time (approximately a few seconds) so that some of channel carriers are injected and trapped in the shallow-level defects within the semiconductor or the semiconductor/insulator interface. Consequently, the drain current decreases and the threshold voltage shifts, rendering the DC $I-V$ method difficult to extract the intrinsic characteristics of the transistor. On the other hand, fast $I-V$ measurements can minimize the effect of trapping by performing a voltage sweep in a relatively short time (approximately 10 μs).[19−21] Figure 3a shows the DC $I-V$ and fast $I-V$ curves of the ITZO TFTs formed with the general DC sputtering method (DC sputtered ITZO TFT) and with the MWA sputtering method (HDP sputtered ITZO TFT). For both the DC sputtered ITZO and HDP sputtered ITZO TFTs, the fast $I-V$ curve shows a higher drain current level and a steeper slope rather than the DC $I-V$ curve. In other words, when measured using the DC $I-V$ method, the transistor transfer characteristic is underestimated due to the fast charge trapping effect, and it is dominant for the ITZO TFT deposited via DC sputtering, representing that the

DOI: 10.1021/acsami.7b08065
ACS Appl. Mater. Interfaces 2017, 9, 36962−36970

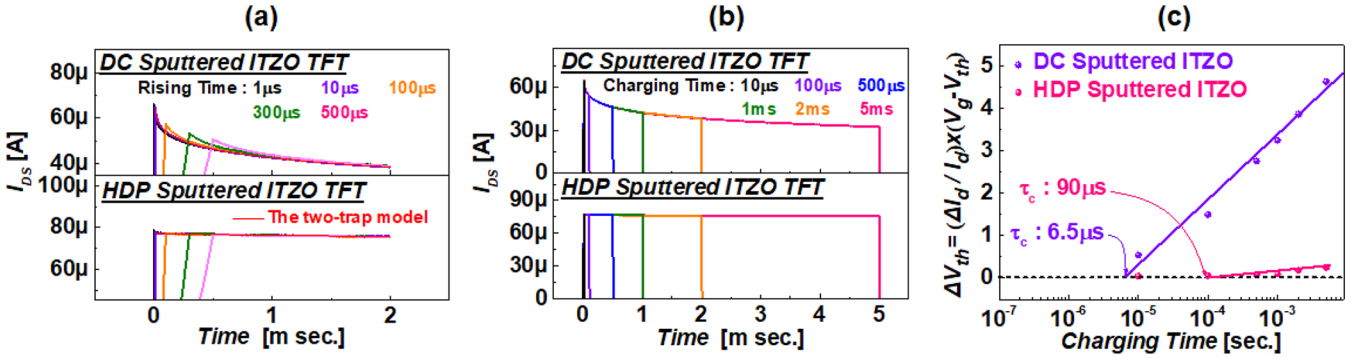

Figure 4. (a) Transient source-to-drain current versus time of DC sputtered ITZO and HDP sputtered ITZO TFTs as a function of rise time from 10 to 500 μs. The red line represents the fitting curve of the two-trap model. (b) Transient source-to-drain current versus time of DC sputtered ITZO and HDP sputtered ITZO TFTs as a function of charge time from 10 μs to 5 ms. (c) ΔV_{th} with charging time for DC sputtered ITZO and HDP sputtered ITZO TFTs and critical time constants extracted by fitting the data.

fast charge trapping effect is prominent in this DC sputtered ITZO TFT.

We performed pulsed $I-V$ measurements on both devices to analyze the current reduction and hysteresis characteristics caused by the fast charge trapping effect as shown in Figure 3b.[22−25] The applying pulse consists of three parts: rising (T_r = 10 μs), width (T_w = 2 ms), and falling (T_f = 10 μs). During the rising pulse, when a voltage of 0−10 V is applied to the gate, electrons are injected from the source and accumulate at the front channel between the gate oxide and the semiconductor. Subsequently, while the pulse of 2 ms is being held, a portion of the carrier accumulated in the channel is trapped in the defect sites near the interface, causing V_{th} shift in the positive bias direction and decrease in the drain current. Figure 3c shows a reduction in the time-dependent current with pulse measurements. Expectedly, typical DC sputtered ITZO TFTs exhibit significant current reduction indicating that charge trapping is dominant in this device, whereas for the HDP sputtered ITZO TFT, the current reduction rarely occurs even during 2 ms of electrical stress. It can be explained by the fact that the ITZO film deposited with HDP is superior in quality and has fewer defect sites inducing minor charge trapping than ITZO film deposited by DC sputter.

To further analyze the fast-transient charging mechanism, we measured the time-dependent transient current for various conditions of rising/falling time and charging time (pulse width) as seen in Figures 4a and 4b. The charge trapping has two different aspects. In the early steps of the decrease of drain current, the current decreases exponentially, which indicates that the carriers will fill the surrounding defect sites in a short period of time.[22] In a longer time scale, the current reduction appears to be gradually and linearly saturated approaching the value related to that of a conventional charge trapping curve. These two different aspects can be explained by a two-trap model with different time constants using eq 1.

$$I = AI_0 \exp\left(-\frac{t}{\tau_A}\right) + BI_0 \exp\left(-\frac{t}{\tau_B}\right) \quad (1)$$

where I_0 is the initial drain current, A and B are the relative ratios of the two processes, and τ_A and τ_B are the short trap time constant and long trap time constant, respectively.[19] The measured data of the transient current can be fitted by this two-trap model and the fitting data is represented in Figure 4a. Since the two-trap model fits the transient current of both the devices, this reveals that charge trapping is evidently controlled by two processes with two different time constants. The time constants (τ_A, τ_B) of both ITZO TFT devices are shown in Table 1. The two time-constants τ_A and τ_B were 92 and 1470 μs, respectively, for the DC sputtered ITZO TFT. The two time-constants τ_A and τ_B were 40 and 3310 μs, respectively, for the HDP sputtered ITZO TFT. Further, the τ_A of the DC ITZO TFT is much larger than that of the HDP sputtered ITZO TFT representing that drain current decays exponentially in the early steps of current reduction owing to the initial fast charge trapping effect. This result indicates that with quantified constants, a new concept of MWA sputter with HDP produces dense and high-quality ITZO films resulting in reduction of charge trapping phenomena during charge transport through the channel. Figure 4c shows the plot of ΔV_{th} with charging time. Further, ΔV_{th} can be determined from the change in the drain current using the following eq 2.[24]

Table 1. Trapping Time Constants Extracted from the Fitting Curve of the Multiple-Trapping Model with Two Trapping Time Constants

active layer	τ_A (μs)	τ_B (μs)
DC Sputtered ITZO	92	1470
HDP Sputtered ITZO	40	3310

$$\Delta V_t = \Delta I_d (V_g - V_t)/I_d \quad (2)$$

This data can be used to predict the critical charge trapping on-set time (τ_C) at which ΔV_{th} is zero and the charge trapping begins. The critical charging times for the DC sputtered ITZO TFT and HDP sputtered ITZO TFT were 6.5 and 90 μs, respectively.

As discussed above, electron trapping occurs during conventional DC $I-V$ measurements, leading to significant underestimation of the mobility values. To estimate the intrinsic mobility of TFT, pulsed $I-V$ with various pulse amplitude approaches is introduced.[22−25] Pulsed $I-V$ measurements are performed on both DC sputtered ITZO TFT and HDP sputtered ITZO TFT with various pulse amplitudes (0, 2, 4, 6, 8, 10 V) as shown in Figures 5a and 5b, respectively. From this data, the threshold voltage shift ΔV_{th} can be determined as a function of the pulse amplitude by using eq 2 as seen in Figure 5c. Further, ΔV_{th} linearly increases with gate pulse bias for both the devices. In other words, the slope of the $\Delta V_{th}-V_{gs}$ graph, that is, $\partial \Delta V_{th}/\partial V_{gs}$ is independent of the gate pulse bias

DOI: 10.1021/acsami.7b08065
ACS Appl. Mater. Interfaces 2017, 9, 36962−36970

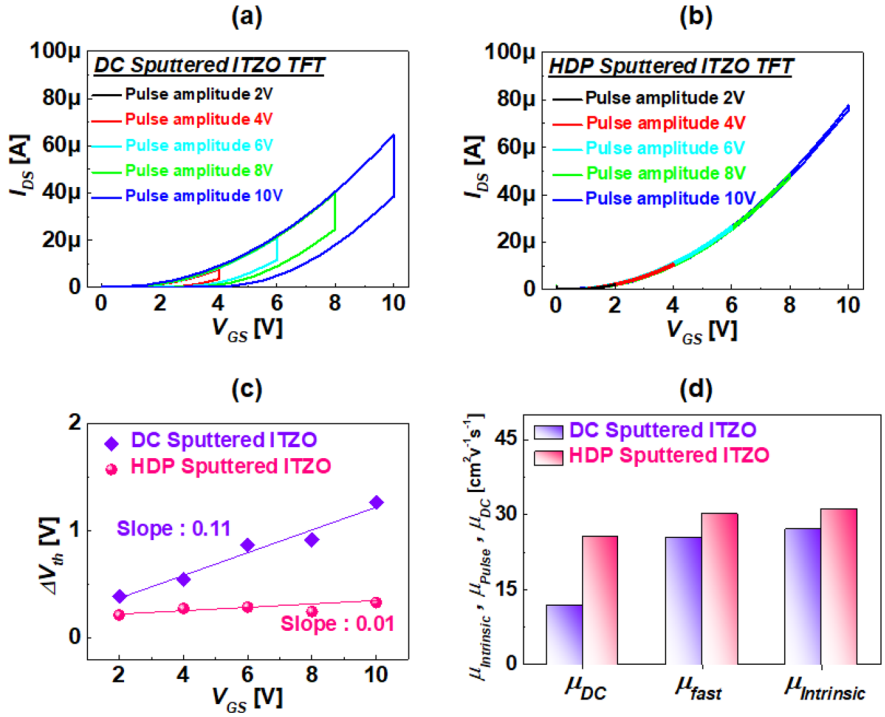

Figure 5. Pulsed $I-V$ curves of (a) DC sputtered ITZO TFT and (b) HDP sputtered ITZO TFT with various pulse amplitudes. (c) The ΔV_{th} versus the pulse amplitude for DC sputtered ITZO and HDP sputtered ITZO TFTs. (d) Conventional DC mobility, μ_{fast} (determined by fast $I-V$) and intrinsic mobility of DC sputtered ITZO and HDP sputtered ITZO TFTs.

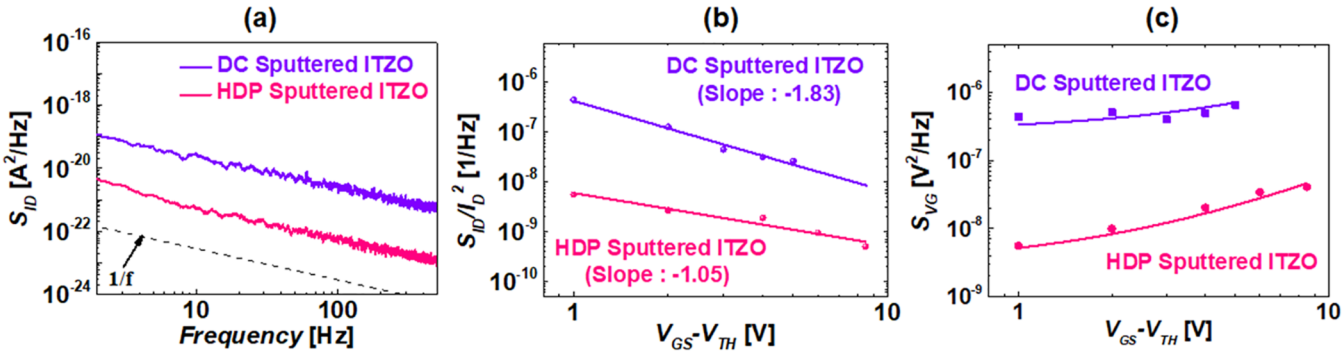

Figure 6. (a) Noise spectral density (S_{ID}) versus frequency for DC ITZO and HDP ITZO TFTs. (b) Normalized noise spectral density (S_{ID}/I_D^2) versus gate overdrive voltage for both TFTs and (c) voltage spectral density (S_{VG}) versus gate overdrive voltage at V_{DS} = 1 V and f = 20 Hz.

in the V_{gs} range of this measurement. The linear relationship between ΔV_{th} and V_{gs} is due to the electron charging effect related to the subgap defect sites in an oxide semiconductor. As the gate voltage increases, the band bending of oxide semiconductors becomes severe leading to significant electron injection and charge trapping and consequently, larger ΔV_{th}. Accordingly, within a small range of gate pulse bias, the amount of charge trapping is approximately linearly increased with gate pulse bias, which explains the constant $\Delta V_{th}-V_{gs}$. As shown in Figure 5c, the slope of the $\Delta V_{th}-V_{gs}$ graph, that is, $\partial\Delta V_{th}/\partial V_{gs}$, was 0.11 and 0.01 for the DC sputtered ITZO TFT and HDP sputtered ITZO TFT, respectively. Finally, we can estimate the intrinsic mobility by utilizing the following eq 3.

$$\mu_a = \mu_i \cdot (1 - \partial\Delta V_{th}/\partial V_{gs}) \quad (3)$$

where μ_a is the measured (apparent) mobility, μ_i is the intrinsic mobility, and $\partial\Delta V_{th}/\partial V_{gs}$ is the slope of the $\Delta V_{th}-V_{gs}$ graph. With this pulsed $I-V$ approach, we can extract the intrinsic mobility, which is not affected by charge trapping effect. Figure 5d summarizes the mobility values extracted by three different methods for both ITZO TFTs: DC $I-V$ measurement, fast $I-V$ measurement, and pulsed $I-V$ approach for intrinsic mobility.

In order to prove the carrier conduction mechanism of both devices, we investigated the low-frequency noise (LFN) properties.[26−28] Figure 6a shows noise spectral densities (S_{ID}) measured at $V_{GS}-V_{th}$ = 1 V and V_{DS} = 1 V. The magnitude of the obtained S_{ID} is appropriate to the $1/f^{\gamma}$ relationship, with γ being approximately 1, obeying the established $1/f$ noise theory. Figure 6b shows the normalized noise current spectral density (S_{ID}/I_D^2) with the gate voltage overdrive $|V_{GS} - V_{th}|$ at 20 Hz to determine the dominant carrier transport mechanism of both devices. As seen in Figure 6b, the normalized S_{ID} is altered as $|V_{GS} - V_{th}|^{-m}$ with m of approximately 1.83 (i.e., close to 2) for the DC sputtered ITZO TFT; the LFN is mainly due to the carrier number fluctuations at the interface between the gate insulator and the semiconductor channel, whereas for HDP sputtered ITZO TFT, S_{ID} is altered as $|V_{GS} - V_{th}|^{-m}$ with m of

DOI: 10.1021/acsami.7b08065
ACS Appl. Mater. Interfaces 2017, 9, 36962−36970

approximately 1.05 (i.e., close to 1), indicating that LFN is primarily responsible for the mobility fluctuations in the front channel.[26−28] From the theory of carrier number fluctuation with correlated mobility fluctuation, we can characterize the input-referred voltage spectral densities ($S_{VG} = S_{ID}/G_M^2$) according to $|V_{GS} - V_{th}|$ as shown in Figure 6c, and it can be translated into the trap density of oxide TFT by applying eqs 4 and 5.

$$S_{VG} = S_{VFB}[1 + \alpha\mu_{eff}C_{ox}(V_{GS} - V_{TH})]^2 \quad (4)$$

$$S_{VFB} = \frac{\lambda kTq^2N_t}{fWLC_{ox}^2} \quad (5)$$

where S_{VFB} is the flat-band voltage noise density, α is the Coulomb-scattering coefficient, μ_{eff} is the effective mobility, C_{ox} is the gate oxide capacitance, λ is the tunneling attenuation coefficient (i.e., approximately 0.11 nm for this device), k is the Boltzmann constant, T is the temperature, q is the elementary charge, N_t is the trap density, and f is the frequency.[29] The extracted parameters are summarized in Table 2. As expected,

Table 2. Extracted Model Parameters of Low-Frequency Noise (LFN)

active layer	N_t (cm^{-3} eV^{-1})	S_{VFB} (V^2/Hz)	α (V·s/C)
DC sputtered ITZO	1.07×10^{19}	2.64×10^{-7}	1.25×10^5
HDP sputtered ITZO	6.13×10^{17}	5.79×10^{-9}	3.14×10^5

N_t of the DC sputtered ITZO TFT was 1.07×10^{19} and N_t of the HDP sputtered ITZO TFT was 6.13×10^{17}. From this result, it is evident that the MWA sputtering method results in fewer defects of film than the traditional method, causing less density of states strongly related to the TFT device performance.

To monitor the defects in the front channel of the oxide TFTs quantitatively, the DCA method was used for the extraction of defect densities in the oxide TFT. This new electrical characterization method is modified from the charge pumping (CP) method, as the CP method is suitable for silicon MOSFETs, which are inversion mode devices, whereas the DCA method is suitable for oxide TFTs, which are accumulation mode devices.[30] Figure 7a shows a schematic of the DCA measurement setup. The DCA method is performed using a pulse generator (Agilent 81104A) and a source meter (Keithley 2401) with Lab-view program. We periodically applied an external pulse bias on the gate while the source and drain were grounded. When we applied gate pulse from V_{th} − 5 V to V_{th} + 10 V, most carriers were injected from the source and drain, and some of the carriers were charged in the defect sites in the front channel of the oxide semiconductor. Subsequently, when the gate pulse was ramping down, most of the free carriers in the front channel were discharged rapidly, whereas the charged carriers trapped in the defect sites were discharged gradually. Therefore, in the pulse off region, there are tail parts of the discharge current (δI), which are induced by the charged carriers released from the defect sites of the oxide TFT. The details of the principle and the related physics of the DCA method were explained in the previous work.[32−34]

To distinguish the free carriers and charged carriers, we measured the discharge current with a gate pulse frequency sweep. As shown in Figure 7b, the discharge current from the defect sites linearly increases with the measurement frequency and finally saturates above a certain frequency. We measured the discharge current by varying the measurement frequency from 100 kHz to 500 kHz, which is the region where the discharge current increases linearly. Subsequently, the slope of the discharge current (I_c)−frequency (f), that is, $\delta I/\delta f$, can be translated into a number of defect sites using eq 6.

$$N_{defectsites}[\text{no./cm}^3] = \frac{2}{k}\cdot\frac{\delta I_c/\delta f}{V\cdot q}\left[\frac{(C/t)\cdot t}{\text{cm}^3\cdot C}\right] \quad (6)$$

where $N_{defectsites}$ is the number of defect sites, k is the charge loss factor used to compensate for the charge loss from the source during measurement, and V is the volume of an active semiconductor.[33] Additionally, we measure the discharge current with various gate pulse amplitudes ($V_{Gamp} = V_G - V_{FB}$). Figure 7c and 7d shows the discharge current as a function of pulse frequency from 100 kHz to 500 kHz by varying the amplitude of gate pulse (V_{Gamp}) of the DC sputtered ITZO TFT and HDP sputtered ITZO TFT, respectively. In the case of the DC ITZO TFT, the slope of I_c−f graph, that is, $\delta I/\delta f$, is very steep compared to that of the HDP ITZO TFT as shown in Figure 7e indicating that many carriers are discharged from the defect sites in the subgap of the DC sputtered ITZO semiconductor. Figure 7f shows the number of defect sites extracted by Eq. 6 with the slope of I_c−f according to the gate voltage amplitude from the conduction band. In addition, the gate voltage can be converted into energy range by using eq 7, and the energy distribution of $N_{defectsites}$ can be obtained as represented in Figure 7g.

$$\phi_s(V_{GS}) = \int_{V_{FB}}^{V_{GS}}\left(1 - \frac{C_G(V_{GS})}{C_i}\right)dV_{GS} \quad (7)$$

By fitting the subgap density profile of exponential tail states and exponential deep states distributed in the energy range using the following DOS model (eq 8), we can extract the model parameters as summarized in Table 3.

$$g(E) = N_{TA}\times\exp\left(-\frac{(E_C - E)}{kT_{TA}}\right) + N_{DA} \times\exp\left(\frac{(E_C - E)}{kT_{DA}}\right) \quad (8)$$

where N_{TA} is the acceptor-like tail state density, kT_{TA} is the acceptor-like tail state characteristic energy, N_{DA} is the acceptor-like deep state density, and kT_{DA} is the acceptor-like deep state characteristic energy.[31] From the result, we also verified that the DC sputtered ITZO TFT has many more acceptor-like states in the subgap than the HDP sputtered ITZO TFT indicating that there are many defects causing significant fast charging effects in the DC sputtered ITZO TFT.

It can be explained by the effect of low operation pressure, which greatly affects the film quality in the sputtering deposition, because various parameters, such as electron temperature and mean free path, depend on the pressure. When we use the MWA sputter, it is possible to process at a high deposition rate even at low working pressure by forming high density plasma. First, when the pressure is low, the electron temperature rises and electrons in the high energy region increase. The energetic electrons activate the ionization and heat up the ions in the plasma. The ions accelerated by the target supply a large ion bombardment energy, causing high sputtering yield and effectively increasing the deposition rate. In

DOI: 10.1021/acsami.7b08065
ACS Appl. Mater. Interfaces 2017, 9, 36962−36970

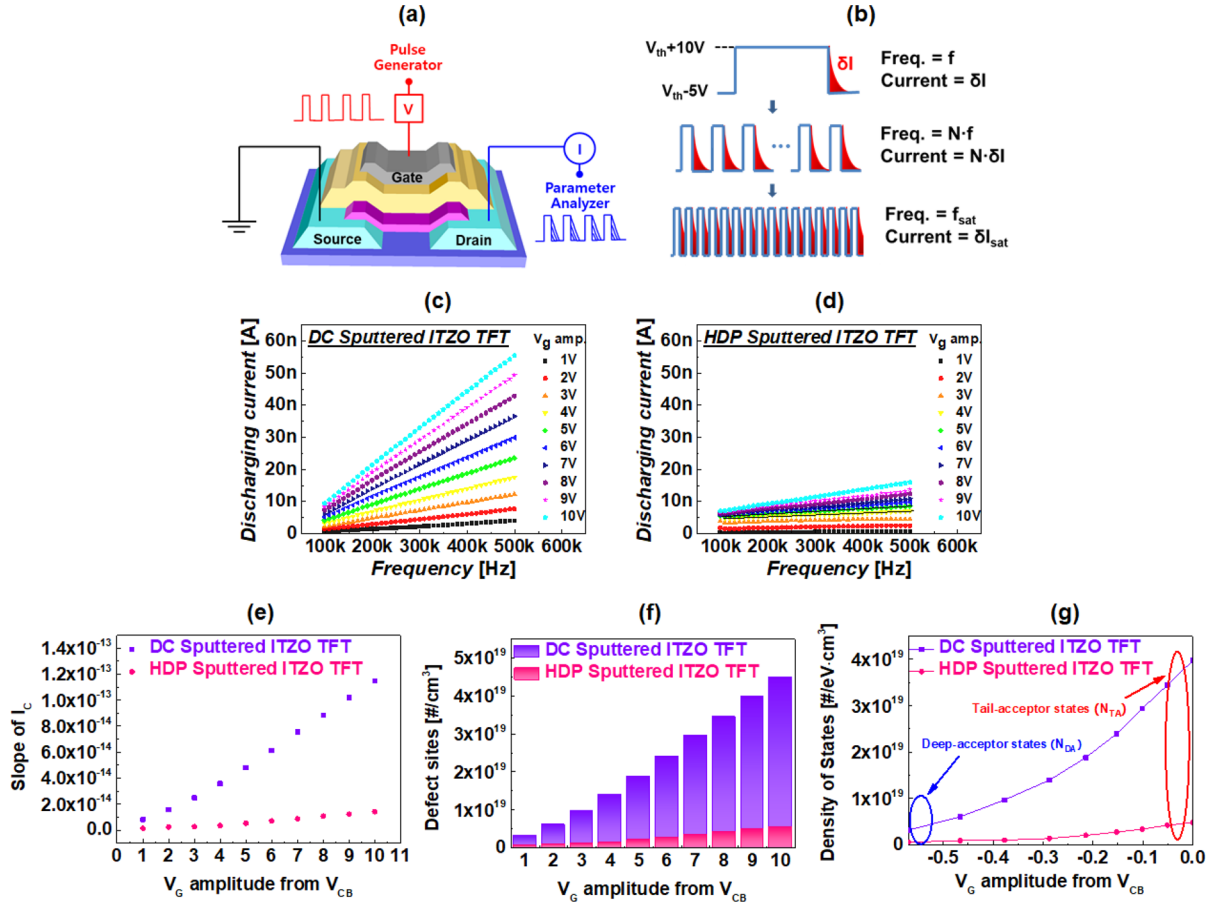

Figure 7. (a) Schematic showing the measurement setup to measure the discharge current. (b) Schematics of pulse showing the amount of discharge current as a function of measurement frequency. As shown in figure, δI increases as the frequency increases. I_c–f measurements for (c) DC ITZO TFT and (d) HDP ITZO TFT with various gate voltage amplitude. (e) Slope of I_c as function of gate voltage amplitude from conduction band. (f) Number of charging sites extracted by the slope of the I_c at a frequency lower than 500 kHz. (g) Density of states of DC ITZO and HDP ITZO TFT extracted by discharging current analysis.

Table 3. Parameters of Subgap Density of States Extracted by Multifrequency *C*–*V* Method

active layer	N_{TA} (cm^{-3} eV^{-1})	kT_{TA} (eV)	N_{DA} (cm^{-3} eV^{-1})	kT_{DA} (eV)
DC sputtered ITZO	4.40×10^{19}	0.38	1.20×10^{19}	0.18
HDP sputtered ITZO	1.58×10^{18}	0.35	8.65×10^{17}	0.11

addition, reflected Ar ions from the target can reach the film with an energy of several tens of eV, which supplies activation energy that facilitates bonding between sputtering atoms.[35] In particular, the MWA sputter has a long mean free path due to low working pressure. When the mean free path is long, reflected Ar ions do not lose energy because of the collision. Therefore, it can provide sufficient activation energy which enables to form the film with high-density, tight binding, and less defect. To accurately perform an analysis, we have calculated the energy of the reflected Ar ions that reach the film in both cases of DC sputter and MWA sputter by using K. Mayer equation (eqs 9–11).[36]

$$E_F = (E_I - k_B T_G)\exp\left[N \cdot \ln\frac{E_f}{E_i}\right] + k_B T_G \tag{9}$$

$$N = \frac{dP_{tot}\sigma}{k_B T_G} \tag{10}$$

$$\frac{E_f}{E_i} = 1 - \frac{\frac{m_{sg}}{m_{sp}}}{\left(1 + \frac{m_{sg}}{m_{sp}}\right)^2} \tag{11}$$

where E_I and E_F is the initial and final energies of energetic particles, $k_B T_G$ is the temperature of sputtering gas, N is the collision number, E_f/E_i is the ratio of energy before and after a collision, d is distance between target and substrate, P_{tot} is the working pressure, and m_{sg} and m_{sp} is atomic weight of sputtering gas and sputtering particle. The final energy of reflected Ar arriving at substrate in case of MWA sputter and conventional DC sputter is 31.8 and 11.2 eV, respectively. From this result, it is clear that by using the MWA sputtering method, more energetically reflected Ar ions supply the activation energy of the film which forms high-density, tight bonds and less defects. Therefore, when the reflected Ar ions effectively supply activation energy, the crystal structure and the density of thin film is enhanced and defects are suppressed resulting in the formation of high-quality and high-performance oxide films.

DOI: 10.1021/acsami.7b08065
ACS Appl. Mater. Interfaces 2017, 9, 36962–36970

4. CONCLUSION

In this Research Article, we introduce the MWA sputter which transfer the microwave and confine high-density plasma by using ECR effect. The MWA sputtering method has the advantages of controllable voltage, low deposition temperatures, and high deposition rate even at low working pressure. Consequently, by utilizing MWA sputtering, it is possible to produce high-quality metal oxide films and improve the electrical characteristics of oxide TFT rendering the most powerful candidates for next-generation display possible. We evaluated the effect of MWA sputtering method on the characteristic of ITZO films by analyzing the defects and fast charge trapping mechanism quantitatively when compared to a typical DC sputtered In−Sn−Zn−O film by using various electrical characterization methods including microsecond fast *I*−*V*, pulsed *I*−*V*, transient current, low frequency noise analysis, and DCA. From the result, we found that the HDP sputtered ITZO exhibited better electrical performance, negligible charge trapping characteristics and low subgap density of states. In MWA system, the working pressure was greatly reduced (0.6 mTorr) compared to the conventional sputtering system (3 mTorr). At low pressure condition, the energetic electrons activate the ionization and heat up the ions in the plasma resulting high deposition rate. In addition, due to long mean free path, reflected Ar ions provide sufficient activation energy which enables to form the film with high density, tight binding and less defect. This study provides the information on defects in oxide device and shows the effect of MWA sputtering system.

AUTHOR INFORMATION

Corresponding Authors

*E-mail: shkp@kaist.ac.kr.

*E-mail: jeonsh@korea.ac.kr.

ORCID

Sanghun Jeon: 0000-0002-4222-1587

Author Contributions

Y.G. and J.A. equally contributed to this work.

Notes

The authors declare no competing financial interest.

ACKNOWLEDGMENTS

This work was supported by the National Research Foundation of Korea (NRF) grant funded by the Korea government (MEST) (No. 2015M3A7B7045496, 2017R1A2A2A05022574) and the Wearable Platform Materials Technology Center (WMC) funded by the National Research Foundation of Korea (NRF) Grant by the Korean Government (MSIP) (No. 2016R1A5A1009926). Also, this work was supported by NRF (National Research Foundation of Korea) Grant funded by the Korean Government (NRF-2017-Fostering Core Leaders of the Future Basic Science Program/Global Ph.D. Fellowship Program) (No. 2017045392).

REFERENCES

(1) Wager, J. F. Transparent electronics. *Science* **2003**, *300*, 1245−1246.

(2) Jeon, S.; et al. Gated three-terminal device architecture to eliminate persistent photoconductivity in oxide semiconductor photosensor arrays. *Nat. Mater.* **2012**, *11*, 301−305.

(3) Lee, S.; Jeon, S.; Chaji, R.; Nathan, A. Transparent Semiconducting Oxide Technology for Touch Free Interactive Flexible Displays. *Proc. IEEE* **2015**, *103*, 644−664.

(4) Jeon, S.; Song, I.; Lee, S.; Ryu, B.; Ahn, S. E.; Lee, E.; Kim, Y.; Nathan, A.; Robertson, J.; Chung, U. I. Origin of High Photoconductive Gain in Fully Transparent Heterojunction Nanocrystalline Oxide Image Sensors and Interconnects. *Adv. Mater.* **2014**, *26*, 7102−7109.

(5) Nomura, K.; Ohta, H.; Takagi, A.; Kamiya, T.; Hirano, M.; Hosono, H. Room-temperature Fabrication of Transparent Flexible Thin-film Transistors Using Amorphous Oxide Semiconductors. *Nature* **2004**, *432*, 488−492.

(6) Kamiya, T.; Nomura, K.; Hosono, H. Present Status of Amorphous In-Ga-Zn-O Thin-film Transistors. *Sci. Technol. Adv. Mater.* **2010**, *11*, 044305−044328.

(7) Lee, E.; Kim, T.; Benayad, A.; Hur, J.; Park, G.-S.; Jeon, S. High mobility and high stability glassy metal-oxynitride materials and devices. *Sci. Rep.* **2016**, *6*, 23940.

(8) Park, J. C.; Kim, S.; Kim, S.; Kim, C.; Song, I.; Park, Y.; Jung, U. I.; Kim, D. H.; Lee, J. S. Highly Stable Transparent Amorphous Oxide Semiconductor Thin-film Transistors Having Double-stacked Active Layer. *Adv. Mater.* **2010**, *22*, 5512−5516.

(9) Cho, D. H.; Yang, S.; Park, S. H. K.; Byun, C.; Yoon, S. M.; Lee, J. H.; Chu, H. Y.; Cho, K. I.; et al. Al and Sn-doped Zinc Indium Oxide Thin Film Transistors for AMOLED Back Plane. *Dig. Tech. Pap. - Soc. Inf. Disp. Int. Symp.* **2009**, *40*, 280−283.

(10) Jeong, J. K. Photo-bias Instability of Metal Oxide Thin Film Transistors for Advanced Active Matrix Displays. *J. Mater. Res.* **2013**, *28*, 2071−2084.

(11) Choi, H.; Jeon, S.; Kim, H.; Shin, J.; Kim, C.; Chung, U. I. Verification of Interface State Properties of a-InGaZnO Thin-film Transistors with and Gate Dielectrics by Low-frequency Noise Measurements. *IEEE Electron Device Lett.* **2011**, *32*, 1083−1085.

(12) Yu, X.; Zhou, N.; Smith, J.; Lin, H.; Stallings, K.; Yu, J.; Marks, T. J.; Facchetti, A. Synergistic Approach to High-performance Oxide Thin Film Transistors Using a Bilayer Channel Architecture. *ACS Appl. Mater. Interfaces* **2013**, *5*, 7983−7988.

(13) Barquinha, P.; Pimentel, A.; Marques, A.; Pereira, L.; Martins, R.; Fortunato, E. Influence of the Semiconductor on the Electrical Properties of Transparent TFTs Based on Indium Zinc Oxide. *J. Non-Cryst. Solids* **2006**, *352*, 1749−1752.

(14) Choi, H. S.; Jeon, S.; Kim, H.; Shin, J.; Kim, C.; Chung, U. I. Influence of Hf Contents on Interface State Properties in a-HfInZnO Thin-film Transistors with SiN_x/SiO_x Gate Dielectrics. *Appl. Phys. Lett.* **2011**, *99*, 183502.

(15) Latz, R.; Daube, C.; Haranou, T.; Ocker, B.; Suzuki, K. Microwave Plasma Assisted Sputtering. *J. Non-Cryst. Solids* **1997**, *218*, 329−334.

(16) Matsuo, S.; Kiuchi, M. Low Temperature Chemical Vapor Deposition Method Utilizing an Electron Cyclotron Resonance Plasma. *Jpn. J. Appl. Phys.* **1983**, *22*, L210−L212.

(17) Ono, T.; Takahashi, C.; Matsuo, S. Electron Cyclotron Resonance Plasma Deposition Technique Using Raw Material Supply by Sputtering. *Jpn. J. Appl. Phys.* **1984**, *23*, L534−L536.

(18) Kubota, E.; Shigesato, Y.; Igarashi, M.; Haranou, T.; Suzuki, K. Effects of Magnetic Field Gradient on Crystallographic Properties in Tin-doped Indium Oxide Films Deposited by Electron Cyclotron Resonance Plasma Sputtering. *Jpn. J. Appl. Phys.* **1994**, *33*, 4997−5004.

(19) Lee, Y.; Kang, C.; Jung, U.; Kim, J.; Hwang, H.; Chung, H.; Seo, S.; Choi, R.; Lee, B. Fast Transient Charging at the Graphene/SiO_2 Interface Causing Hysteretic Device Characteristics. *Appl. Phys. Lett.* **2011**, *98*, 183508.

(20) Jung, H. Y.; Kang, Y.; Hwang, A. Y.; Lee, C. K.; Han, S.; Kim, D. H.; Bae, J. U.; Shin, W. S.; Jeong, J. K. Origin of the Improved Mobility and Photo-bias Stability in a Double-channel Metal Oxide Transistor. *Sci. Rep.* **2015**, *4*, 3765.

(21) Shen, C.; Li, M. F.; Wang, X. P.; Yeo, Y.-C.; Kwong, D. L. A Fast Measurement Technique of MOSFET Id−Vg Characteristics. *IEEE Electron Device Lett.* **2006**, *27*, 55−57.

DOI: 10.1021/acsami.7b08065
ACS Appl. Mater. Interfaces 2017, 9, 36962−36970

(22) Kim, T.; Hur, J. H.; Jeon, S. Pulse I–V Characterization of a Nano-crystalline Oxide Device with Sub-gap Density of States. *Nanotechnology* **2016**, *27*, 215203.
(23) Kim, T.; Choi, R.; Jeon, S. Influence of Fast Charging on Accuracy of Mobility in a-InHfZnO Thin-Film Transistor. *IEEE Electron Device Lett.* **2017**, *38*, 203–206.
(24) Young, C. D.; Zhao, Y.; Heh, D.; Choi, R.; Lee, B.; Bersuker, G. Pulsed I_d-V_g Methodology and its Application to Electron-trapping Characterization and Defect Density Profiling. *IEEE Trans. Electron Devices* **2009**, *56*, 1322–1329.
(25) Kim, T.; Hur, J. H.; Jeon, S. Fast Transient Charging Behavior of HfInZnO Thin-film Transistor. *Appl. Phys. Lett.* **2015**, *107*, 093503.
(26) Choi, H.; Jeon, S.; Kim, H.; Shin, J.; Kim, C.; Chung, U. I. The Impact of Active Layer Thickness on Low-frequency Noise Characteristics in InZnO Thin-film Transistors with High Mobility. *Appl. Phys. Lett.* **2012**, *100*, 173501.
(27) Lee, J. M.; Cheong, W. S.; Hwang, C. S.; Cho, I. T.; Kwon, H. I.; Lee, J. H. Low-Frequency Noise in Amorphous Indium-Gallium-Zinc-Oxide Thin-film Transistors. *IEEE Electron Device Lett.* **2009**, *30*, 505–507.
(28) Jeon, S.; Kim, S. I.; Park, S.; Song, I.; Park, J.; Kim, S.; Kim, C. Low-Frequency Noise Performance of a Bilayer InZnO-InGaZnO Thin-film Transistors for Analog Device Applications. *IEEE Electron Device Lett.* **2010**, *31*, 1128–1130.
(29) Choi, H. S.; jeon, S.; Kim, H.; Shin, J.; Kim, C.; Chung, U. I. Verification of Interface State Properties of *a*-InGaZnO Thin-film Transistors with SiN_x and SiO_2 Gate Dielectrics by Low-frequency Noise Measurements. *IEEE Electron Device Lett.* **2011**, *32*, 1083–1085.
(30) Jung, U.; Lee, Y. G.; Kang, C. G.; Lee, S.; Kim, J. J.; Hwang, H. J.; Lim, S. K.; Ham, M. H.; Lee, B. H. Quantitatively Estimating Defects in Graphene Devices Using Discharge Current Analysis Method. *Sci. Rep.* **2015**, *4*, 4886.
(31) Lee, S.; Park, S.; Kim, S.; Jeon, Y.; Jeon, K.; Park, J. H.; Park, J.; Song, I.; Kim, C. J.; Park, Y.; Kim, D. M.; Kim, D. H. Extraction of Subgap Density of States in Amorphous InGaZnO Thin-film Transistors by Using Multifrequency Capacitance-voltage Characteristics. *IEEE Electron Device Lett.* **2010**, *31*, 231–233.
(32) Jia, J.; Torigoshi, Y.; Shigesato, Y. In Situ Analyses on Negative Ions in the Indium-Gallium-Zinc Oxide Sputtering Process. *Appl. Phys. Lett.* **2013**, *103*, 013501.
(33) Jia, J.; Torigoshi, Y.; Kawashima, E.; Utsuno, F.; Yano, K.; et al. Amorphous Indium-Tin-Zinc Oxide Films Deposited by Magnetron Sputtering with Various Reactive Gases: Spatial Distribution of Thin Film Transistor Performance. *Appl. Phys. Lett.* **2015**, *106*, 023502.
(34) Carcia, P. F.; Mclean, R. S.; Reilly, M. H.; Li, Z. G.; et al. Influence of Energetic Bombardment on Stress, Resistivity, and Microstructure of Indium Tin Oxide Films Grown by Radio Frequency Magnetron Sputtering on Flexible Polyester substrates. *J. Vac. Sci. Technol., A* **2003**, *21*, 745–751.
(35) Yamamura, Y.; Ishida, M. Monte Carlo Simulation of the Thermalization of Sputtered Atoms and Reflected Atoms in the Magnetron Sputtering Discharge. *J. Vac. Sci. Technol., A* **1995**, *13*, 101.
(36) Meyer, K.; Schuller, I. K.; Falco, C. M. Thermalization of Sputtered Atoms. *J. Appl. Phys.* **1981**, *52*, 5803.

DOI: 10.1021/acsami.7b08065
ACS Appl. Mater. Interfaces 2017, 9, 36962–36970